available at www.sciencedirect.com

ScienceDirect

journal homepage: www.sciencedirect.com/journal/chinese-journal-of-catalysis

Article

Insights into effects of ZrO_2 crystal phase on syngas-to-olefin conversion over ZnO/ZrO_2 and SAPO-34 composite catalysts

Zhaopeng Liu [a,b,c], Youming Ni [a,b], Zhongpan Hu [a,b], Yi Fu [a,b,c], Xudong Fang [a,b,c], Qike Jiang [a,b], Zhiyang Chen [a,b,c], Wenliang Zhu [a,b,*], Zhongmin Liu [a,b,c,#]

[a] *National Engineering Laboratory for Methanol to Olefins, Dalian Institute of Chemical Physics, Chinese Academy of Sciences, Dalian 116023, Liaoning, China*

[b] *Dalian National Laboratory for Clean Energy, Dalian Institute of Chemical Physics, Chinese Academy of Sciences, Dalian 116023, Liaoning, China*

[c] *University of Chinese Academy of Sciences, Beijing 100049, China*

ARTICLE INFO

Article history:
Received 18 June 2021
Accepted 23 July 2021
Available online 5 xxxxxx 2021

Keywords:
Syngas-to-olefins
Crystal phase
ZnO/ZrO_2
SAPO-34
Composite catalyst

ABSTRACT

The utilization of metal oxide-zeolite catalysts (OX-ZEO) in the syngas-to-olefin (STO) reaction is a promising strategy for producing C_2–C_4 olefins from non-petroleum resources. However, the effect of the crystal phase of metal oxides on the catalytic activity of these oxides is still ambiguous. Herein, typical metal oxides (ZnO/ZrO_2) with different crystal phases (monoclinic (*m*-ZrO_2) and tetragonal (*t*-ZrO_2)) were employed for syngas conversion. The (ZnO/*m*-ZrO_2+SAPO-34) composite catalyst exhibited 80.5% selectivity for C_2–C_4 olefins at a CO conversion of 27.9%, where the results are superior to those (CO conversion of 16.4% and C_2–C_4 olefin selectivity of 76.1%) obtained over (ZnO/*t*-ZrO_2+SAPO-34). The distinct differences are ascribed to the larger number of hydroxyl groups, Lewis acid sites, and oxygen defects in ZnO/*m*-ZrO_2 compared to ZnO/*t*-ZrO_2. These features result in the formation of more formate and methoxy intermediate species on the ZnO/*m*-ZrO_2 oxides during syngas conversion, followed by the formation of more light olefins over SAPO-34. The present findings provide useful information for the design of highly efficient ZrO_2-based catalysts for syngas conversion.

1. Introduction

Light olefins ($C_{2-4}^{=}$), the chief building block chemicals of modern industry, are generally produced from the catalytic cracking of petroleum-derived naphtha [1–3]. Owing to the growing demand for light olefins, there is an urgent need to develop an alternative technique for producing light olefins from non-petroleum resources such as coal, natural gas, or biomass. Syngas is a key non-petroleum carbon resource and has been successfully transformed into olefins in China *via* indirect syngas-to-methanol and subsequent methanol-to-olefin (MTO) processes [4–6]. Recently, more attention has been focused on the direct conversion of syngas to olefins because this process involves fewer operation units [7–9], resulting in lower capital costs and higher profits than the MTO process. The traditional direct process for synthesizing light olefins is based on Fischer-Tropsch (FT) synthesis. However, the products are limited by the Anderson-Schulz-Flory distribution, and the

* Corresponding author. Tel/Fax: +86-411-84379418; E-mail: wlzhu@dicp.ac.cn
# Corresponding author. E-mail: liuzm@dicp.ac.cn
This work was supported by the National Natural Science Foundation of China (21978285, 21991093, 21991090), and the "Transformational Technologies for Clean Energy and Demonstration", Strategic Priority Research Program of the Chinese Academy of Sciences (XDA21030100).
DOI: 10.1016/S1872-2067(21)63908-6 | http://www.sciencedirect.com/journal/chinese-journal-of-catalysis | Chin. J. Catal., Vol. 42, No. 0, xxxxxx 2021

selectivity for C_2–C_4 hydrocarbons is below 58% [7,9–11].

Recently, another route for the direct conversion of syngas to olefins (STO) involving the metal oxide-zeolite composite catalyst (OX-ZEO STO) was developed by Bao *et al*. [8]. The $ZnCrO_x$/MSAPO composite catalyst yielded 80% $C_{2-4}^{=}$ [8,12] at a CO conversion of 17%. Later, Wang's group reported another $ZnZrO_x$/SAPO-34 composite catalyst, which afforded approximately 70% $C_{2-4}^{=}$ *via* syngas conversion. These two studies opened a new avenue for the highly selective conversion of syngas or CO_2 to light olefins. Zn-based oxides such as $ZnCrO_2$ [8,13], $ZnZrO_2$ [12,14], $ZnCeZrO_2$ [15], and $InZrO_2$ [16] combined with SAPO-34 have been widely applied in this field. $ZnZrO_2$ oxide has received extensive attention, and great progress has been made with this catalyst owing to its good performance in CO or CO_2 activation. ZrO_2 adopts two different crystal phases, monoclinic (*m*-ZrO_2) and tetragonal (*t*-ZrO_2), which affect the catalytic performance during CO conversion. However, there is no systematic study on the effect of the crystal phase of ZrO_2 on STO conversion. Understanding the structure-performance relationship would facilitate the design of more efficient catalysts.

In this study, we synthesize ZnO/*m*-ZrO_2 and ZnO/*t*-ZrO_2 catalysts and apply them in the STO reaction after mixing with SAPO-34. (ZnO/*m*-ZrO_2+SAPO-34) affords 80% C_2–C_4 olefin selectivity at a CO conversion of 27.9% under conditions of 648 K, 1.5 MPa, H_2/CO ratio = 2, and space velocity = 2500 mL g^{-1} h^{-1}. This performance is superior to that of (ZnO/*t*-ZrO_2+SAPO-34). ZnO/*m*-ZrO_2 possesses more hydroxyl groups, Lewis acid sites, and oxygen defects than ZnO/*t*-ZrO_2 and yields more formate and methoxy intermediate species during CO conversion, which favors the formation of light olefins over SAPO-34.

2. Experimental

2.1. Catalyst preparation

Zirconium nitrate hydrate ($ZrO(NO_3)_2{\cdot}xH_2O$, 45 mol% in zirconia base, Aladdin), urea (≥45 units/mg dry weight, Kermel), methanol (Standard for GC, >99.9%, Aladdin), and zinc nitrate ($Zn(NO_3)_2{\cdot}xH_2O$, 99 wt%, Kermel) were commercial reagents and were used directly without further processing.

The ZrO_2 supports were synthesized using the hydrothermal/solvothermal method [17]. As a typical synthesis, *m*-ZrO_2 was prepared by a hydrothermal method. Briefly, 9.26 g of $ZrO(NO_3)_2{\cdot}xH_2O$ was dissolved in 80 mL of deionized water, followed by adding 24.08 g of urea under vigorous stirring for 0.5 h. The synthesis gel was placed in a 120 mL Teflon-lined stainless steel autoclave, which was kept at 463 K for 32 h under static conditions. The resulting precipitate was separated by centrifugation, dried at 110 °C for 12 h, and then ground to prepare the catalyst as a support precursor. Methanol was used as a solvent for synthesizing *t*-ZrO_2 using the same procedure as that used for the synthesis of *m*-ZrO_2. Both samples were further calcined at 600 °C for 4 h at a heating rate of 2 °C/min to obtain *m*-ZrO_2 and *t*-ZrO_2 for characterization.

ZnO/ZrO_2 catalysts were prepared by incipient wetness impregnation of the as-synthesized ZrO_2 support precursors. The obtained catalysts containing monoclinic and tetragonal ZnO/ZrO_2 are denoted as ZnO/*m*-ZrO_2 and ZnO/*t*-ZrO_2, respectively.

The composite catalyst (ZnO/ZrO_2+SAPO-34) containing ZnO/m-ZrO_2 or ZnO/*t*-ZrO_2 oxide and SAPO-34 was prepared by simple mechanical mixing of the granules (0.4–0.8 mm) of the two components. The weight ratio of the oxide and zeolite for the composite catalysts was 2:1.

2.2. Evaluation of catalytic performance

The experiments were conducted in a fixed-bed stainless steel reactor. Before each catalytic activity test, 0.3 g of the oxide-zeolite catalyst with a particle size of 20–40 mesh was loaded in the middle of the reactor and fixed with quartz wool. The catalyst was subsequently pretreated under H_2 for 2 h at 673 K at a flow rate of 20 mL/min, under atmospheric pressure. The STO reaction conditions were as follows: syngas composition: H_2/CO = 2/1, gas hourly space velocity 2500 mL g^{-1} h^{-1}, 1.5 MPa. The product effluent was kept in the gas phase and analyzed online using an Agilent 7890 B GC equipped with an HP-PLOT/Q capillary column connected to a FID detector and a TDX-1 column connected to a TCD detector. Methane was used as a reference bridge between the TCD and FID. Argon was used as the inner standard. The hydrocarbon selectivities were based on the number of carbon atoms. The CO conversion and CO_2 selectivity were calculated using the following equations:

$$\text{CO conversion (\%)} = (CO_{in} - CO_{out})/CO_{in} \times 100$$

$$CO_2 \text{ selectivity (\%)} = CO_{2,out}/(CO_{in} - CO_{out}) \times 100$$

CO_{in}: moles of CO in feedstock, CO_{out}: moles of CO in products, $CO_{2,out}$: moles of CO_2 in products.

The selectivity for the hydrocarbons (C_nH_m), DME or MeOH was determined based on the total carbon atoms in the products, as detected by FID.

$$C_nH_m \text{ selectivity (\%)} = C_nH_{m,out}/\sum C_nH_{m,out} \times 100$$

$$\text{MeOH selectivity (\%)} = MeOH_{out}/\textit{total carbon atoms of products} \times 100$$

$$\text{DME selectivity (\%)} = MeOH_{out}/\textit{total carbon atoms of products} \times 100$$

$C_nH_{m,out}$: carbon atom number of C_nH_m detected by FID; $MeOH_{out}$: carbon atom number of MeOH detected by FID; DME_{out}: carbon atom number of DME detected by FID.

2.3. Characterization of catalysts

The X-ray diffraction (XRD) patterns were obtained using a PANalytical X'Pert PRO X-ray diffractometer with Cu-K_α radiation. Elemental analysis was carried out using a Philips Magix-601 X-ray fluorescence (XRF) spectrometer. The BET surface areas, average pore width, and pore volumes of all the samples were estimated from the nitrogen adsorption-desorption isotherms acquired at 77 K using a Micromeritics ASAP 2020 apparatus. The nanostructure of the ZnO/ZrO_2 catalysts was determined using a Tecnai G2F20 (200 kV) high-resolution transmission electron microscope (HRTEM) (FEI, Holland) equipped with an X-ray microprobe

with 0.14 nm optimum resolution for energy dispersive X-ray spectroscopy (EDS). X-ray photoelectron spectroscopy (XPS) was performed using a Thermo Fisher ESCALAB 250Xi spectrometer. CO-temperature-programmed desorption (*in situ* CO-TPD) of the samples was conducted using a 2910 automatic chemical adsorption instrument (Micromeritics, United States) in the temperature range from room temperature to 973 K with a ramp of 10 K/min; the desorption products were monitored by mass spectroscopy *in situ*.

The *in situ* diffuse reflection infrared Fourier-transform spectroscopy (DRIFTS) studies were carried out on a Bruker Tensor 27 instrument with an MCT detector to detect changes in the intensity of surface intermediate species. The sample powder was pressed into a diffuse reflectance infrared cell with a ZnSe window. The DRIFTS profile of adsorbed CO and syngas (H_2/CO = 2:1) was recorded using an *in situ* cell. For these experiments, 50 mg of the sample powder was placed in the cell. Prior to adsorption, the sample was dried at 573 K in N_2 for 2 h. CO was adsorbed *in situ* for 20 min at different temperatures. Spectra were recorded with a Nicolet FTIR spectrometer with a resolution of 2 cm^{-1} and a scan number of 32. The surface hydroxyl groups of the samples were evaluated using the same DRIFTS instrument and a similar pretreatment process. Pyridine adsorption on the catalyst was performed using a Nicolet 6700 FTIR spectrometer equipped with a TGS detector. The sample (15 mg) was pressed into a self-supporting wafer and treated in a quartz cell at 573 K under vacuum for 2 h. After exposure to pyridine vapor at ambient temperature for 30 min, the wafer was outgassed at 423 K for 1 h, after which IR spectra were collected with a resolution of 4 cm^{-1} and a scan number of 32. The organic materials retained in SAPO-34 after the reactions were analyzed by Guisnet's method [18]. The spent SAPO-34 zeolites were dissolved in 20 wt% HF solution. After neutralization with 5 wt% sodium hydroxide solution, the soluble organics were extracted with CH_2Cl_2 (containing 10 ppm C_2Cl_6 as an inner standard) and then analyzed using a GC-MS instrument (Agilent 7890 B) equipped with a HP-5 capillary column.

3. Results and discussion

3.1. Catalytic performance

The composite catalysts (ZrO_2+SAPO-34) and (ZnO/ZrO_2+SAPO-34) were used for the STO reaction. The results are presented in Table 1 and Fig. S1(a). The composite catalyst (*m*-ZrO_2+SAPO-34) generated 82.1% C_2–C_4 olefins at a CO conversion of 3.6%, which is higher than that of the (*t*-ZrO_2+SAPO-34) catalyst (with only 0.5% CO conversion and 76.5% C_2–C_4 olefin selectivity). After loading 12 wt% ZnO into the composite (Table S1), the CO conversion over the resulting (ZnO/*t*-ZrO_2+SAPO-34) catalyst increased to 14.6% without sacrificing the C_2–C_4 olefin selectivity. Surprisingly, the CO conversion reached 22.4% over (ZnO/*m*-ZrO_2+SAPO-34), with a selectivity higher than 84% for C_2–C_4 olefins.

This suggests that the (ZnO/*m*-ZrO_2+SAPO-34) composite catalyst not only promotes CO conversion, but also favors the formation of olefins. The catalytic performance of the (ZnO/*m*-ZrO_2+SAPO-34) composite catalyst under different reaction conditions was also investigated. As shown in Fig. 1(a), when the reaction pressure was increased from 1.0 to 1.5 MPa, the CO conversion increased from 22.4% to 27.9%, and the C_2–C_4 olefins remained at approximately 80.1%. To the best of our knowledge, this CO conversion is the best reported thus far and was achieved at a lower reaction pressure (< 2.0 MPa) compared to other studies on STO, with a C_2–C_4 olefin selectivity > 80% (Table S2) [8,12,13,16,19–23]. After further increasing the reaction pressure to 2.0 MPa, the selectivity for olefins was less than 80%; thus, high pressure is not conducive to achieving high selectivity for light olefins. Overall, increasing the reaction pressure is beneficial to CO conversion but disadvantageous to the formation of C_2–C_4 olefins, owing to the hydrogenation of C_2–C_4 olefins at higher reaction pressure [24,25]. The CO conversion could be enhanced at relatively high reaction temperatures, with lower C_2–C_4 olefin selectivity (Fig. 1(b)). Typically, upon increasing the reaction temperature from 648 to 683 K, the CO conversion increased from 27.9% to 33.9%, but the C_2–C_4 olefin selectivity decreased dramatically from 80.1% to 62.1%. More than 80% C_2–C_4 olefin selectivity with 27.9% CO conversion was obtained at a reaction temperature of 648 K, whereas a reaction temperature below 648 K did not favor CO conversion and C_2–C_4 olefin selectivity. In addition to the hydrocarbon products, MeOH and DME were detected as major products at 623 K, indicating that MeOH and DME might be intermediates of the STO reaction. Fig. S1(b) shows that the CO conversion increased linearly with increasing H_2/CO ratio, whereas an excessively high H_2/CO ratio was not conducive for achieving higher selectivity for C_2–C_4 olefins due to the hydrogenation of olefins. Increasing the space velocity can also help to promote the generation of C_2–C_4 olefins, but does not favor CO conversion. Furthermore, the MeOH and DME selectivities increased slightly with increasing space velocity (shown in Fig. S1(c)). This suggests that the formation of olefins over the (ZnO/*m*-ZrO_2+SAPO-34) composite catalyst proceeded *via* methanol and DME as intermediates. The weight ratio of ZnO/*m*-ZrO_2 oxide and SAPO-34 was studied, where the

Table 1
Catalytic STO conversion over various composite catalysts.

Composite catalyst	CO Conversion (%)	CO_2 Selectivity (%)	Hydrocarbon distribution (%)			
			CH_4	C_2–$C_4^=$	C_2–C_4^o	C_{5+}
t-ZrO_2+SAPO-34	0.5	undetected	9.1	76.6	12.2	2.1
m-ZrO_2+SAPO-34	3.6	42.2	2.3	82.3	12.6	2.7
ZnO/*t*-ZrO_2+SAPO-34	14.6	44.2	2.4	79.4	16.4	1.8
ZnO/*m*-ZrO_2+SAPO-34	22.4	44.8	1.7	84.5	11.5	2.2

Reaction conditions: 648 K, 1.0 MPa, 2500 mL g^{-1} h^{-1}, H_2/CO molar ratio = 2/1, weight ratio of OX/ZEO = 2:1.

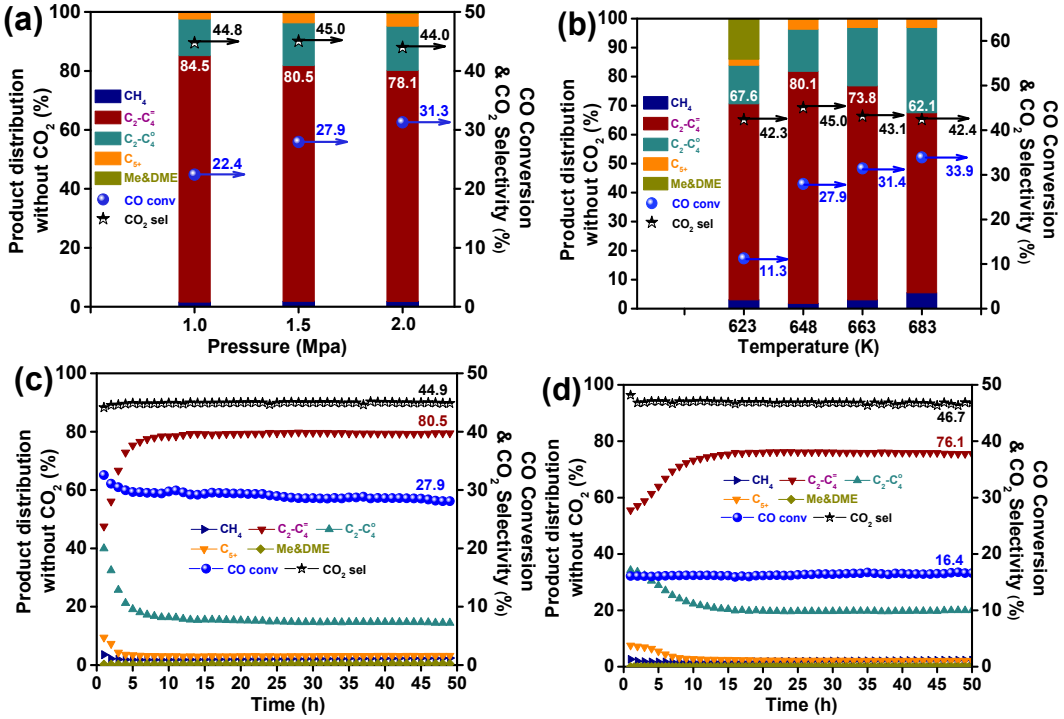

Fig. 1. Catalytic STO conversion over (ZnO/ZrO_2+SAPO-34) composite catalysts. (a) Effect of reaction pressure (648 K, 2500 mL g^{-1} h^{-1}, H_2/CO molar ratio = 2/1); (b) effect of reaction temperature (1.5 MPa, 2500 mL g^{-1} h^{-1}), H_2/CO molar ratio = 2/1); stability of STO reactions over (ZnO/*m*-ZrO_2+SAPO-34) (c) and (ZnO/*t*-ZrO_2+SAPO-34) (d), (648 K, 1.5 MPa, 2500 mL g^{-1} h^{-1}, H_2/CO molar ratio = 2/1).

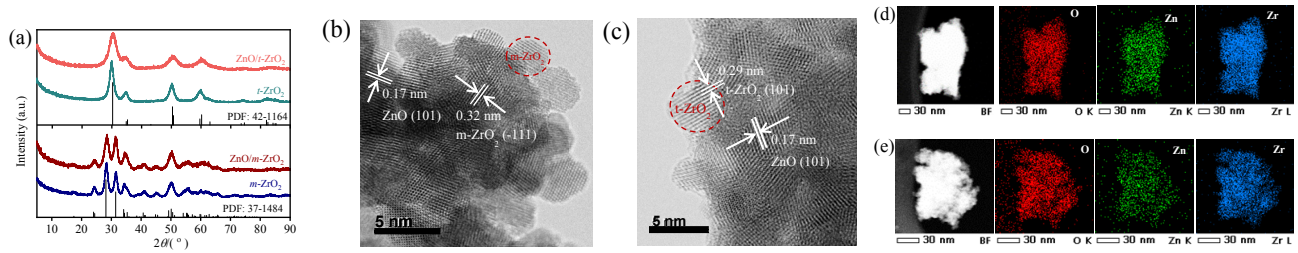

Fig. 2. Structural characterization. (a) XRD patterns; (b,c) HRTEM images of ZnO/*m*-ZrO_2 and ZnO/*t*-ZrO_2 catalysts; (d,e) elemental mapping of ZnO/*m*-ZrO_2 and ZnO/*t*-ZrO_2 catalysts.

optimal weight ratio was 2:1 (Fig. S1(d)). Fig. S1(e) shows the spatial arrangement of the different active components. The closer proximity of these components, induced by changing the manner of integration from dual-bed to granule mixing, can significantly increase both the CO conversion and formation of lower olefins. Upon further increasing the intimate mixing of the two components, the CO conversion increased slightly, while the selectivity for lower olefins declined.

After the above optimization, the composite catalyst (ZnO/*m*-ZrO_2+SAPO-34) demonstrated good stability during the 50 h test under the following conditions: 648 K, 1.5 MPa, H_2/CO molar ratio of 2, and space velocity of 2500 mL g^{-1} h^{-1} (Fig. 1(c)). The CO conversion was nearly 10% higher than that achieved with the (ZnO/*t*-ZrO_2+SAPO-34) composite catalyst (Fig. 1(d)). The C_2–C_4 olefin selectivity over the former composite catalyst was higher than that of the latter. This proves that as a metal oxide support, *m*-ZrO_2 is better than *t*-ZrO_2 for the STO reaction.

3.2. Structural characterization

The XRD profiles of the ZrO_2 supports and ZnO/ZrO_2 catalysts are shown in Fig. 2(a), illustrating the typical peaks of *m*-ZrO_2 (JCPDS NO. 37-1484) and *t*-ZrO_2 (JCPDS NO. 42-1164), respectively. The XRD patterns of the ZnO/ZrO_2 metal catalysts were similar to those of the ZrO_2 supports. No diffraction peaks of ZnO species were found in the profiles of the ZnO/ZrO_2 catalysts, suggesting that ZnO was well dispersed on the ZrO_2 supports. Table S1 summarizes the structural properties of the supports and the catalysts. The introduction of 12 wt% ZnO (see XRF results) resulted in a slight decrease in the ZrO_2 particle size. Similarly, the BET surface area of the ZnO/ZrO_2 catalysts decreased after ZnO loading, which may be due to the dispersion of ZnO in the pores of ZrO_2. The UV-vis diffuse reflectance spectra of all the samples (including the ZrO_2 supports and ZnO/ZrO_2 catalysts) are shown in Fig. S2. As in pre-

vious reports [26], the ZnO crystallites absorbed strongly in this range, where the onset of absorption for all the synthesized ZnO/ZrO_2 catalysts was near 370 nm due to the small ZnO crystals. Figs. 2(b) and (c) shows the HRTEM images of the ZnO/ZrO_2 catalysts, where ZrO_2 exhibits a spherical morphology. The monoclinic ZrO_2 is mainly enclosed by the (−111) plane, while tetragonal ZrO_2 is mainly enclosed by the (101) plane. A lattice fringe spacing of 0.17 nm, assigned to the (101) plane of crystalline ZnO, was found, which indicates the formation of crystalline ZnO on the surface of the ZrO_2 supports. Considering the XRD, UV-vis diffuse reflectance spectra, and HRTEM data, it was confirmed that ZnO crystals were the primary components in all ZnO/ZrO_2 catalysts and were highly dispersed on the surface of the ZrO_2 supports. This viewpoint is also supported by EDS mapping. No obvious aggregation was observed in the ZnO/*m*-ZrO_2 and ZnO/*t*-ZrO_2 catalysts (Figs. 2(e) and (f)). Moreover, the EDS maps and XRF results for these two crystal ZnO/ZrO_2 metal catalysts were similar (Table S3), which further illustrates that ZnO species were uniformly dispersed on the ZrO_2 supports.

The FTIR spectra in Fig. 3(a) and Fig. S3(a) show three bands at 3566, 3745, and 3765 cm^{-1} for the *t*-ZrO_2 and ZnO/*t*-ZrO_2 oxides, assigned to tri-bridged, bi-bridged, and terminal hydroxyl groups, respectively [27,28]. The hydroxyl groups on the *m*-ZrO_2 and ZnO/*m*-ZrO_2 oxides are predominantly bi-bridged and *tri*-biridged. Notably, the FTIR peaks ascribed to the hydroxyl groups of the *m*-ZrO_2 and ZnO/*m*-ZrO_2 catalysts were more intense than those of their tetragonal counterparts (Fig. S3). This suggests that the differences in the surface hydroxyl groups are caused by the ZrO_2 crystal structure. The monoclinic ZnO/ZrO_2 catalyst contained more OH groups. This result is also confirmed by the dehydration signals of these two catalysts, as shown in Fig. S5(a). It is well known that a higher concentration of OH groups on Zr-based catalysts not only promotes the reaction of CO with OH groups, leading to the formation of carboxylate species, but also facilitates the formation of defect oxygen [29]. O 1*s* XPS analysis was performed to investigate the oxygen defects. As shown in Fig. 3(b) and Fig. S3(b), the O 1*s* XPS profiles of the ZrO_2 supports and the corresponding ZnO/ZrO_2 catalysts clearly show two peaks. These two peaks at 531.6 and 529.6 eV are attributed to lattice and defect oxygen, respectively [30]. Table S4 shows that the amount of defect oxygen in the *m*-ZrO_2 and ZnO/*m*-ZrO_2 catalysts exceeded that in the tetragonal counterparts, which is consistent with the relative content of surface hydroxyl groups determined by FTIR spectroscopy. More oxygen defects on ZnO/*m*-ZrO_2 promote CO activation, as confirmed by the CO-FTIR analysis presented below.

The FTIR spectra after pyridine adsorption on these two crystal ZnO/ZrO_2 metal oxides are shown in Fig. 3(c). The FTIR signals of the Lewis acid sites at 1445, 1490, and 1606 cm^{-1} [31] were distinctly observed in the profiles of these two ZnO/ZrO_2 metal catalysts. ZnO/*m*-ZrO_2 exhibited a higher density of acid sites than ZnO/*t*-ZrO_2. Recent investigations have shown that the larger number of Lewis acid sites in ZrO_2-based oxides is attributed to the presence of a high concentration of anion vacancies [32,33], which is consistent with the catalytic performance of the STO reaction over these two (ZnO/ZrO_2+SAPO-34) composite catalysts. The *in situ* DRIFTS profiles of adsorbed CO were used to determine the influence of the crys-

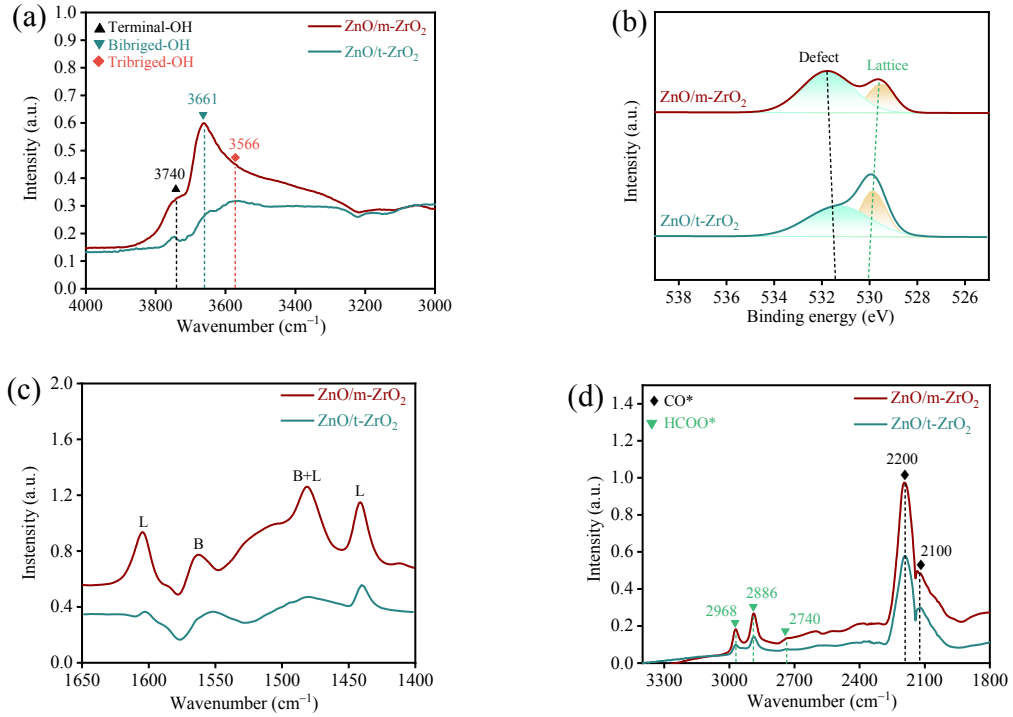

Fig. 3. FT-IR and XPS data. (a) FTIR spectra of ZnO/ZrO_2 catalysts; (b) O 1*s* XPS profiles of ZnO/ZrO_2 catalysts; (c) FTIR spectra of ZnO/ZrO_2 catalysts after pyridine adsorption and evacuation at 423 K; (d) DRIFTS profiles after CO adsorption at 643 K.

tal phases of zirconia on CO conversion. For these experiments, the ZnO/*t*-ZrO_2 and ZnO/*m*-ZrO_2 catalysts were purged with pure CO for 20 min to establish steady-state. As shown in Fig. 3(d) and Fig. S6, adsorbed CO (2100, 2200 cm^{-1}) and carboxylate (2740, 2886, and 2968 cm^{-1}) [21,34,35] were the main species observed on these two ZnO/ZrO_2 catalysts after the adsorption of CO. The signal intensity for these species on the surface of ZnO/*m*-ZrO_2 was remarkably higher than that on the ZnO/*t*-ZrO_2 surface in the temperature range of 623–673 K, which suggests that ZnO/*m*-ZrO_2 forms stronger bonds with CO than ZnO/*t*-ZrO_2 [21,35]. This difference indicates that ZnO/*m*-ZrO_2 is more favorable for CO adsorption and activation.

The results of *in situ* CO-TPD analysis also support this viewpoint, as shown in Fig. S5(b). The amount of CO_2 generated from adsorbed CO in the reaction catalyzed by ZnO/*m*-ZrO_2 was approximately twice that obtained with the ZnO/*t*-ZrO_2 catalyst. It has been reported that in the absence of hydrogen, CO_2 mainly comes from the decomposition of formates, which are created by the reaction of adsorbed CO with surface hydroxyl groups [35,36]. According to the analysis above, we speculate that ZnO/*m*-ZrO_2 metal oxide with more oxygen defects (associated with the hydroxyl groups) can contribute to enhancing the catalyst performance for CO conversion. As a result, the (ZnO/*m*-ZrO_2+SAPO-34) catalyst exhibited better catalytic performance than the (ZnO/*t*-ZrO_2+SAPO-34) catalyst for the STO reaction.

Based on previous reports, the STO reaction over the OX-ZEO composite catalyst occurs *via* a formate-methoxy pathway. Hence, in order to gain further insight into the effect of the ZrO_2 crystal phases on syngas conversion over the ZnO/ZrO_2 and (ZnO/ZrO_2+SAPO-34) catalysts, the formation and evolution of key intermediates were monitored by *in-situ* DRIFTS (Fig. 4). The adsorbed surface carbonate/bicarbonate species (1492, 1380, and 1305 cm^{-1}) [20,34,35], formate species [23,34,37,38] (2957, 2867, 2743, 1580, and 1357 cm^{-1}), and methoxy species [34,37,38] (2930, 2820, 1152, and 1052 cm^{-1}) were distinctly observed in these ZnO/ZrO_2 and (ZnO/*m*-ZrO_2+SAPO-34) composite catalysts under the reaction conditions. Noticeably, more of these intermediate species were present on the ZnO/*m*-ZrO_2 catalyst than on ZnO/*t*-ZrO_2,

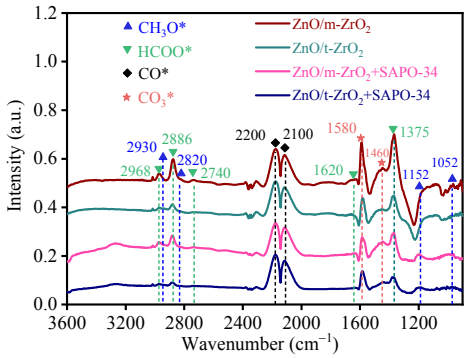

Fig. 4. *In-situ* DRIFT spectra for syngas conversion over various catalysts. Reaction conditions: 648 K, 0.1 MPa, syngas refers to the mixed gas of $CO/H_2/Ar$ = 31.7/63.3/5.

and the intensity of the signals of the intermediate species in the composite catalyst (ZnO/*m*-ZrO_2+SAPO-34) was higher than that of (ZnO/*t*-ZrO_2+SAPO-34). The larger quantity of intermediate species may result in excellent CO conversion over (ZnO/*m*-ZrO_2+SAPO-34). The results of *in situ* DRIFTS are in accordance with the catalytic behaviors shown in Fig. 1(c) and Fig. 1(d), respectively. Therefore, the (ZnO/*m*-ZrO_2+SAPO-34) composite catalyst is more advantageous for the STO reaction. In addition, the signals of all the above species became less intense after the introduction of SAPO-34 into the ZnO/ZrO_2 catalysts, which suggests that the active surface intermediates generated over the ZnO/ZrO_2 catalysts can be further consumed by SAPO-34. Remarkably, methoxy is considered a crucial intermediate for methanol synthesis and is mainly produced by hydrogenation of formate species. Therefore, the syngas-to-olefin conversion over the ZnO/ZrO_2+SAPO-34 composite catalysts was confirmed to follow a formate-methoxy route.

To further confirm the mechanism of the STO reaction, the soluble carbonaceous deposits in the SAPO-34 zeolite in the (ZnO/ZrO_2+SAPO-34) composite catalysts after the reaction were analyzed by GC–MS. The organic species retained in the SAPO-34 component are analogous (Fig. S7), and some methylbenzenes were observed, such as methylnaphthalenes and phenanthrene, which are considered as the "hydrocarbon pool" intermediates [39]. Hence, the MTO reaction occurred in the presence of the (ZnO/ZrO_2+SAPO-34) catalysts *via* methanol synthesis, followed by MTO reactions (Fig. S8), where (ZnO/*m*-ZrO_2+SAPO-34) exhibited excellent performance in this process.

4. Conclusions

In summary, ZnO/*m*-ZrO_2 and ZnO/*t*-ZrO_2 composite catalysts were prepared by impregnation of the ZrO_2 support containing different crystal phases (monoclinic and tetragonal structures) with zinc nitrate solution. After mixing with SAPO-34, the composite catalysts were employed for syngas conversion to produce light olefins. The $C_{2-4}^{=}$ selectivity and CO conversion reached 80.5% and 27.9%, respectively, over (ZnO/*m*-ZrO_2+SAPO-34), which are much higher than those over (ZnO/*t*-ZrO_2+SAPO-34). Compared with ZnO/*t*-ZrO_2, ZnO/*m*-ZrO_2 has more hydroxyl groups, Lewis acid sites, and oxygen defects, which favor the generation of formate and methoxy intermediate species, thereby improving the catalytic performance of the composite catalyst. This research can guide the design of highly active ZrO_2-based catalysts for syngas conversion.

Author contributions

All authors contributed to this work. All authors have given approval to the final version of the paper.

Declaration of Competing Interest

The authors declare no competing financial interest.

Acknowledgments

We acknowledge Weichen Zhang for his help in experiment. We acknowledge Mrs. Yanli He and Mr. Yijun Zheng for their help in the characterization of catalysts. We acknowledge Prof. Peng Guo for his kind assistance in the TEM test.

Electronic supporting information

Supporting information is available in the online version of this article.

References

[1] A. Corma, F. V. Melo, L. Sauvanaud, F. Ortega, *Catal. Today*, **2005**, 107–108, 699–706.
[2] G. Centi, E. A. Quadrelli, S. Perathoner, *Energy Environ. Sci.*, **2013**, 6, 1711–1731.
[3] R. Diercks, J. D. Arndt, S. Freyer, R. Geier, O. Machhammer, J. Schwartze, M. Volland, *Chem. Eng. Technol.*, **2010**, 31, 631–637.
[4] P. Tian, Y. X. Wei, M. Ye, Z. M. Liu, *ACS Catal.*, **2015**, 5, 1922–1938.
[5] X. Wu, S. T. Xu, W. N. Zhang, J. D. Huang, J. Z. Li, B. W. Yu, Y. X. Wei, Z. M. Liu, *Angew. Chem. Int. Ed.*, **2017**, 56, 9039–9043.
[6] M. Yang, D. Fan, Y. X. Wei, P. Tian, Z. M. Liu, *Adv. Mater.*, **2019**, 31, 1902181.
[7] W. Zhou, K. Cheng, J. C. Kang, C. Zhou, V. Subramanian, Q. H. Zhang, Y. Wang, *Chem. Soc. Rev.*, **2019**, 48, 3193–3228.
[8] F. Jiao, J. Li, X. L. Pan, J. Xiao, H. Li, H. Ma, M. Wei, Y. Pan, Z. Zhou, M. Li, S. Miao, J. Li, Y. Zhu, D. Xiao, T. He, J. Yang, F. Qi, Q. Fu, X. H. Bao, *Science*, **2016**, 351, 1065–1068.
[9] L. S. Zhong, F. Yu, Y. An, Y. Zhao, Y. H. Sun, Z. Li, T. Lin, Y. Lin, X. Qi, Y. Dai, L. Gu, J. Hu, S. Jin, Q. Shen, H. Wang, *Nature*, **2016**, 538, 84–100.
[10] H. M. Galvis, J. H. Bitter, C. B. Khare, R. Matthijs, D. A. Iulian, K. P. De Jong, *Science*, **2012**, 335, 835–838.
[11] R. A. Friedel, R. B. Anderson, *J. Am. Chem. Soc.*, **1950**, 72, 1212–1215.
[12] A. Chatupheeraphat, H.-H. Liao, S. Mader, M. Sako, H. Sasai, I. Atodiresei, M. Rueping, *Angew. Chem., Int. Ed.*, **2016**, 55, 4803–4806.
[13] J. Su, H. Zhou, S. Liu, C. Wang, W. Jiao, Y. Wang, C. Liu, Y. Ye, L. Zhang, Y. Zhao, H. Liu, D. Wang, W. M. Yang, Z. K. Xie, M. He, *Nat. Commun.*, **2019**, 10, 1297.
[14] M. Wang, Z. Wang, S. Liu, R. Gao, Y. Wang, *J. Catal.*, **2020**, 394, 181–192.
[15] S. Wang, P. Wang, D. Shi, S. He, L. Zhang, W. Yan, Z. Qin, J. Li, M. Dong, J. Wang, U. Olsbye, W. B. Fan, *ACS Catal.*, **2020**, 10, 2046–2059.
[16] J. Su, D. Wang, Y. Wang, H. Zhou, C. Liu, S. Liu, C. Wang, W. M. Yang, Z. K. Xie, M. Y. He, *ChemCatChem*, **2018**, 10, 1536–1541.
[17] W. Li, H. Huang, H. Li, W. Zhang, H. Liu, *Langmuir*, **2008**, 24, 8358–8366.
[18] M. Guisnet, P. Magnoux, *Appl. Catal.*, **1989**, 54, 1–27.
[19] Y. Huang, H. Ma, Z. Xu, W. Qian, W. Ying, *Fuel*, **2020**, 273, 117771.
[20] N. Li, F. Jiao, X. L. Pan, Y. Ding, J. Feng, X. H. Bao, *ACS Catal.*, **2019**, 9, 960–966.
[21] Y. Zhu, X. L. Pan, F. Jiao, J. Li, J. Yang, M. Ding, Y. Han, Z. Liu, X. Bao, *ACS Catal.*, **2017**, 7, 2800–2804.
[22] G. Raveendra, C. Li, B. Liu, Y. Cheng, F. Meng, Z. Li, *Catal. Sci. Technol.*, **2018**, 8, 3527–3538.
[23] X. Liu, W. Zhou, Y. Yang, K. Cheng, J. Kang, L. Zhang, G. Zhang, X. Min, Q. Zhang, Y. Wang, *Chem. Sci.*, **2018**, 9, 4708–4719.
[24] J. Kanal, J. A. Martens, P. A. Jacobs, *J. Catal.*, **1992**, 133, 527–543.
[25] S. Senger, L. Radom, *J. Am. Chem. Soc.*, **2000**, 122, 2613–2620.
[26] G. Liu, L. Zeng, Z. J. Zhao, H. Tian, T. F. Wu, J. L. Gong, *ACS Catal.*, **2016**, 6, 2158–2162.
[27] K. T. Jung, A. T. Bell, *J. Mol. Catal. A*, **2000**, 163, 27–42.
[28] L. Passauer, K. Salzwedel, M. Struch, N. Herold, J. Appelt, *ACS Sustain. Chem. Eng*, **2016**, 4, 6629–6637.
[29] P. M. D. Souza, R. C. Rabelo-Neto, L. E. P. Borges, G. Jacobs, B. H. Davis, U. M. Graham, D. E. Resasco, F. B. Noronha, *ACS Catal.*, **2015**, 5, 7385–7398.
[30] Z. P. Liu, Y. Xu, J. M. Cheng, W. H. Wang, B. W. Wang, Z. H. Li, X. B. Ma, *Appl. Surf. Sci.*, **2018**, 433, 730–738.
[31] S. Song, L. Di, G. Wu, W. Dai, N. Guan, L. Li, *Appl. Catal. B*, **2017**, 205, 393–403.
[32] M. C. Campa, G. Ferraris, D. Gazzoli, I. Pettiti, D. Pietrogiacomi, *Appl. Catal. B*, **2013**, 142–143, 423–431.
[33] C. Liu, W. H. Wang, Y. Xu, Z. H. Li, B. W. Wang, X. B. Ma, *Appl. Surf. Sci.* **2018**, 441, 482–490.
[34] C. Zhou, J. Shi, W. Zhou, K. Cheng, Q. H. Zhang, J. C. Kang, Y. Wang,

Graphical Abstract

Chin. J. Catal., 2021, 42: 0–0 doi: 10.1016/S1872-2067(21)63908-6

Insights into effects of ZrO_2 crystal phase on syngas-to-olefin conversion over ZnO/ZrO_2 and SAPO-34 composite catalysts

Zhaopeng Liu, Youming Ni, Zhongpan Hu, Yi Fu, Xudong Fang, Qike Jiang, Zhiyang Chen, Wenliang Zhu *, Zhongmin Liu *
Dalian Institute of Chemical Physics, Chinese Academy of Sciences; University of Chinese Academy of Sciences

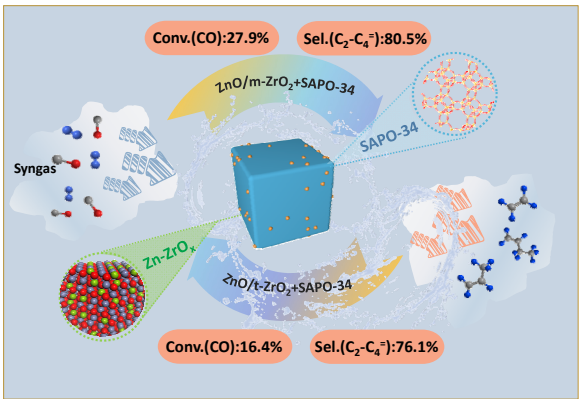

Monoclinic ZnO/ZrO_2 oxide mixed with SAPO-34 zeolite (ZnO/*m*-ZrO_2+SAPO-34) exhibited higher CO conversion and selectivity for C_2–C_4 olefins, with values much higher than those achieved with tetragonal (ZnO/*t*-ZrO_2+SAPO-34) in the STO conversion.

ACS Catal. **2020**, 10, 302–310.
[35] K. Pokrovski, K. T. Jung, A. T. Bell, *Langmuir*, **2001**, 17, 4297–4303.
[36] J. Paier, C. Penschke, J. Sauer, *Chem. Rev.*, **2013**, 113, 3949–3985.
[37] M. T. Arslan, B. Ali, S. Z. A. Gilani, Y. Hou, F. B. Wei, *ACS Catal.*, **2020**, 10, 2477–2488.
[38] Z. Y. Chen, Y. M. Ni, F. Wen, Z. Q. Zhou, W. L. Zhu, Z. M. Liu, *Chin. J. Caltal.*, **2021**, 42, 835–843.
[39] Z. P. Liu, Y. M. Ni, T. T. Sun, W. L. Zhu, Z. M. Liu, *J. Energy Chem.*, **2021**, 54, 111–117.

ZrO_2晶相对ZnO/ZrO_2+SAPO-34双功能催化剂上合成气制烯烃反应的影响研究

刘朝鹏[a,b,c], 倪友明[a,b], 胡忠攀[a,b], 傅怡[a,b,c], 房旭东[a,b,c], 蒋齐可[a,b], 陈之旸[a,b,c], 朱文良[a,b,*], 刘中民[a,b,c,#]

[a]中国科学院大连化学物理研究所, 甲醇制烯烃国家工程实验室, 辽宁大连116023
[b]中国科学院大连化学物理研究所, 洁净能源国家实验室(筹), 辽宁大连116023
[c]中国科学院大学, 北京100049

摘要: 烯烃是重要的化工原料, 目前主要通过石油催化裂化得到. 随着石油资源的消耗以及人们对烯烃需求日益增长的, 开发非石油路线制取烯烃势在必行. 合成气可以由煤、天然气和生物质等获得, 基于合成气作为重要的C1平台分子一步制取烯烃(STO)的过程得到了广泛的关注. 通过将合成气制甲醇/二甲醚的金属催化剂与甲醇制烯烃的分子筛催化剂耦合得到的混合双功能催化剂, 合成气可以高选择性转化为烯烃. 其中, ZnO/ZrO_2金属氧化物催化剂被广泛应于合成气的活化, 然而, 氧化物结构对混合催化剂上合成气制烯烃的影响尚不明确. 本文合成了单斜相*m*-ZrO_2和四方相*t*-ZrO_2, 并负载ZnO制成催化剂, 再将其与SAPO-34分子筛物理混合得到混合双功能催化剂, 并用于合成气制烯烃反应中. 在较优化的条件下, ZnO/*m*-ZrO_2与分子筛组成的双功能催化剂上CO转化率为27.9%, 低碳烯烃选择性达80%, 性能明显优于ZnO/*t*-ZrO_2+SAPO-34双功能催化剂.

为了研究ZrO_2晶相对其催化合成气制烯烃反应性能的影响, 本文对ZnO/ZrO_2进行红外光谱表征. 结果表明, ZnO/*m*-ZrO_2较ZnO/*t*-ZrO_2具有更多的表面羟基和更多的路易斯酸性位点. 金属氧化物表面的路易酸主要是与催化剂表面不饱和的金属离子有关, 而且Zr基催化剂表面羟基有助于缺陷氧的形成, 因此, ZnO/*m*-ZrO_2催化剂表面应该具有更高浓度的氧缺陷位. 光电子能谱进一步证明了ZnO/*m*-ZrO_2表面具有更高浓度的氧缺陷位. 另外, Zr基催化剂上表面羟基还有利于CO与其形成羧酸盐物种, 在350~400 ºC CO原位吸附的红外表征表明, ZnO/*m*-ZrO_2催化剂上CO吸附的浓度及其表面羧酸盐浓度均明显高于ZnO/*t*-ZrO_2催化剂, 这与ZnO/*m*-ZrO_2具有更好的合成气转化性能一致.

为了探究该催化剂体系中合成气制烯烃的反应路径, 分别对两种晶相的ZrO_2和相应的双功能催化剂进行了原位红外监测. 与CO红外漫反射相比, 合成气氛围下金属氧化的表面除了存在吸附态的CO和甲酸盐物种, 还存在表面甲氧基物种, 后者是合成气制甲醇/二甲醚过程重要的中间物种. 本文同样对合成气制烯烃过程的分子筛部分残留的物种进行分析, 结果发现, 残留物种中含有多甲基苯、多甲基萘等甲醇制烯烃过程中的烃池物种. 另外, 合成气氛围下双功能催化剂甲氧基信号峰明显弱于金属氧化物表面甲氧基的信号强度, 表明STO过程应该是合成气制甲醇/二甲醚与甲醇制烯烃的串联过程.

综上所述, 在STO反应中, 相较于ZnO/*t*-ZrO_2催化剂, ZnO/*m*-ZrO_2催化剂具有更高浓度的表面羟基物种、路易斯酸密度和表面氧缺陷位, 从而有利于羧酸盐及甲氧基中间物种的形成, 进而提高了双功能催化剂上STO反应性能.

关键词: 合成气制烯烃; 晶相; ZnO/ZrO_2; SAPO-34; 双功能催化剂

收稿日期: 2021-06-18. 接受日期: 2021-07-23. 上网时间: 2021-00-05.
*通讯联系人. 电话/传真: (0411)84379418; 电子信箱: wlzhu@dicp.ac.cn
#通讯联系人. 电子信箱: liuzm@dicp.ac.cn
基金来源: 国家自然科学基金(21978285, 21991093, 21991090); 中国科学院A类战略性先导科技专项课题（XDA21030100）.
本文的电子版全文由Elsevier出版社在ScienceDirect上出版(http://www.sciencedirect.com/journal/chinese-journal-of-catalysis).